Covalently and ionically, dually crosslinked chitosan nanoparticles block quorum sensing and affect cell growth on a cell-density dependent manner

Vila-Sanjurjo C[1,2§], Hembach L. [1†§], Netzer J.[1], Remuñán-López C.[2], Vila-Sanjurjo A.[3], Goycoolea F.M.[1,5]**

[1]*Westfälische Wilhelms Universität Münster. IBBP. Laboratory of Nanobiotechnology. Schlossplatz 8. Münster, 48143. Germany*

[2]*Department of Pharmacy and Pharmaceutical Technology. Universidade de Santiago de Compostela. Campus Vida, s/n, 15782 Santiago de Compostela Spain*

[4]*Grupo GIBE. Departamento de Bioloxía e Centro de Investigacions Científicas Avanzadas (CICA), Universidade da Coruña (UDC). Campus Zapateira, s/n, 15071 A Coruña, Spain.*

[5]*School of Food Science and Nutrition. University of Leeds. Leeds LS2 9JT. United Kingdom*

Present affiliation: † Westfälische Wilhelms Universität Münster. IBBP. Laboratory of Molecular Phytopathology and Renewable Resources. Schlossplatz 8. Münster, 48143. Germany

§ These authors have contributed equally to this publication

*Authors for correspondence: F.M.Goycoolea@leeds.ac.uk; antonvila.s@gmail.com

KEYWORDS:

Chitosan, nanoparticles, quorum sensing, quorum quenching, genipin, percolation theory.

ABSTRACT

In our efforts to improve the quality and stability of chitosan nanoparticles (NPs), we describe here a new type of chitosan NPs dually crosslinked with genipin and TPP, which display quorum quenching activity. These NPs, named PC-NPs, were created by means of a simplified and robust procedure that resulted in improved physico-chemical properties and enhanced stability. This procedure involves the covalent crosslinking of chitosan with genipin, followed by the formation of chitosan nanoparticles by ionic gelation with TPP. We have optimized the conditions to obtain genipin *p*re-*c*rosslinked *n*ano*p*articles (PC-NPs) with positive zeta-potential ($\zeta \sim +30$ mV), small diameter (~130 nm) and low size distributions (PdI = 0.1 - 0.2). PC-NPs present physicochemical properties that are comparable to those of other dually crosslinked chitosan NPs fabricated with different protocols. In contrast to these NPs, we found that PC-NPs strongly reduce the AHL-mediated quorum sensing response of an *E. coli* fluorescent biosensor. Thus, PC-NPs combine, in a single design, the stability of dually crosslinked chitosan NPs and the quorum quenching activity of ionically crosslinked NPs. Similar to other chitosan NPs, the mode of action of PC-NPs is consistent with the existence of a "stoichiometric ratio" of NP/bacterium, at which the negative ζ-potential potential of the bacterial envelope is counteracted by the positive charge of the NPs. Notably, we found that the time of the establishment of the "stoichiometric ratio" is a function of the NP concentration, implying that these NPs could be ideal for applications in which the targeting of bacterial populations at specific cell densities is desired. We are confident that our PC-NPs are up-and-coming candidates for the design of efficient anti-quorum sensing and a new generation antimicrobial strategies.

INTRODUCTION

Chitosan (CS) is a family of cationic and biodegradable aminopolysaccharide polymers derived from partial deacetylation of chitin. The physical and chemical properties of CS are mainly determined by the relative abundance of deacetylated units and by their molecular weight. This versatility makes CS a solid candidate for applications in the food, cosmetic, pharmaceutical and biomedical fields [1]. Physical or chemical crosslinking is frequently applied to improve the physicochemical properties of CS and tune them to the design of efficient CS-based biopharmaceuticals [2–4]. Ionic crosslinking normally involves polyanions, such as sodium tripolyphosphate (TPP), which interact with the protonated amine-groups of CS [5–9]. Chemical crosslinking of CS has been reported to increase its stability against pH, temperature and biological and mechanical degradation [3,4,10–12]. Genipin (GNP) is a natural covalent crosslinker derived from the geniposide compound found in the fruits of *Gardenia spp*. GNP is receiving intense attention as it constitutes a more compatible and less cytotoxic alternative to covalent crosslinkers such as glutaraldehyde [13–16]. The crosslinking reaction between GNP and CS occurs in two steps. First, a nucleophilic attack of a CS primary amine group to the GNP C3 carbon atom leads to the formation of a heterocyclic compound linked to a glucosamine residue. This reaction is followed by a slower nucleophilic substitution of the GNP ester group (C11), the formation of a secondary amide linkage with CS, and the formation of crosslinking bridges [15]. The degree of covalent crosslinking with GNP can be controlled to modulate specific properties of CS-based materials, such as the release of biomolecules, the stability against pH and temperature variations, or the structure of the CS gel network. Due to all these properties, GNP-based crosslinking of CS is the subject of an increasing number of applications in the fields of Material Sciences, Biotechnology and Pharmaceutical Technology [11,13,17–21].

Quorum sensing (QS) is a cell-to-cell signaling mechanism mediated by exocellular chemical compounds which act as autoinducers. QS is reported to control a number of bacterial phenotypes, from bioluminescence to antibiotic production, biofilm formation and secretion of virulence factors, among others [22–25]. In Gram-negative bacteria, the molecular family of the acyl-homoserine lactones (AHLs) constitute the most abundant species of autoinducers [26,27]. AHLs are synthesized by LuxI-type enzymes and can freely diffuse in and out of the cell, where they bind to LuxR-type regulators of QS gene expression [28,29]. Since QS is deeply involved in the development of pathogenicity in bacteria, the search for anti-QS strategies, or quorum quenching (QQ), is a growing field of interest. QQ strategies normally include the use of agents capable to block QS molecular mechanisms. As such, QQ can occur by the inactivation of either the autoinducer, its receptor, or the AHL synthase [23,30–37]. Regarding CS, research on its potential to interfere with QS is growing quickly [11,38–41].

In a recent paper [42], we reported the ability of ionically crosslinked CS nanoparticles (NPs) using TPP (IC-NPs), to interfere with QS. Despite their QQ activity, IC-NPs displayed high polydispersity and low colloidal stability in microbiological medium. As a first attempt to overcome this, we crosslinked IC-NPs with GNP and found that this treatment led to the formation of a core-shell ultrastructure that stabilized the system, albeit with a significant decrease of their QQ activity [42]. While the resulting NPs, hereafter named CC-NPs, were potentially useful in contexts in which QQ is not desired, we set out to find new formulations that combined the stability of CC-NPs with the QQ activity of IC-NPs. In the present work, we found that by reversing the preparation protocol to first crosslinking of CS with GNP close to the critical gelling condition, followed by ionotropic formation of NPs in the presence of TPP, resulted in NPs displaying improved physico-chemical features while retaining the QQ and antimicrobial activity. This, along with the fact that the fabrication process is faster and more

robust, made us confident that these NPs could serve as the chassis for the development of CS-based nanomaterials intended for microbiological applications. We named these genipin *p*re-*c*rosslinked *NP*s (PC-NPs). In addition, we show here that PC-NPs have the potential to target bacterial populations in a cell-density specific manner. This feature could be used for the targeting of bacterial populations at specific stages of growth.

EXPERIMENTAL SECTION

Materials

High-purity grade CS in its hydrochloride salt form (Protasan UP CL113) was purchased from Novamatrix (FMC-Biopolymer, Norway). CS´s MW was ~92 kDa, *PD (Mw/Mn)* ~2.5, as determined by GPC-MALLS-DRI; and the degree of acetylation (DA) was ~14%, as determined by ^{1}H NMR. GNP was purchased from Challenge Bioproducts Co. Ltd. (Touliu, Taiwan). TPP, N-(3-oxo-hexanoyl)-L-homoserine lactone (3OC6HSL, named AHL hereafter), and other chemicals were purchased from Merck KGaA, (Darmstadt, Germany). Milli-Q water was used throughout. All reagents were of analytical grade.

Chemical pre-crosslinking of CS with GNP

Prior to the preparation of the mixtures of CS- and GNP (CS/GNP), stock solutions of CS (2 mg/mL) and GNP (5 mg/mL), were prepared directly in 85 mM NaCl, sterile-filtered through a 0.22-µm membrane, and stored at 4 ºC until use. This type of chitosan has been manufactured to allow its easy dissolution in water [43]. To assess the optimal composition and consistency of the CS/GNP mixture, different GNP:CS mass ratios were screened. To this end, working solutions of CS (2 mg/mL) and GNP (0.12, 0.24 and 0.48 mg/mL) were first prepared in 85 mM NaCl. Next, aliquots of the two components were mixed in a final volume of 30 mL in order to

obtain CS/GNP mixtures with 0.06:1, 0.12:1 and 0.24:1 GNP:CS mass ratios. The mixtures were incubated for 72 h in capped, 100-mL Erlenmeyer flasks at 37 ºC in an orbital shaker (100 rpm).

The kinetics of the crosslinking reaction was monitored by UV/VIS spectroscopy (V-630 UV-VIS Spectrophotometer, JASCO Corporation, Tokyo, Japan) (λ=200-900 nm) and by dynamic light scattering using non-invasive back scattering (DLS-NIBS) with a Malvern Zetasizer NanoZS ZEN 3600, (Malvern Panalytical, UK); equipped with a red 4mW He/Ne laser output operating at λ= 633 nm. In both cases, 1 mL-aliquots of the CS/GNP mixtures were transferred to measurement cuvettes at specific time points, spanning a total of 72 h of sample incubation. The samples were measured in triplicates and each one of them was measured three times at 37 ºC. After each measurement, the aliquots were returned to the batch solution.

To estimate the critical gel time, the DLS-NIBS intensity correlation data were approximated by percolation kinetics [44]. First, the intensity correlation function $g^{(2)}$ (t_D)-1 was fitted to the modified exponential stretched KWW function, as explained in de Morais et. al [45]. Thus, the initial part of the DLS correlograms, expressed as the correlation coefficients *vs*. delay times (t_D), was fitted to the KWW-based stretched exponential equation (Equation 1) with Origin Pro 8 (OriginLab, Northampton, MA):

$$g^{(2)}(t_D) - 1 = 1 - \beta e^{-(2\Gamma_c t_D)} \quad (1)$$

where β is a constant that depends on the optical properties of the system and and Γ_c is the relaxation rate [45].

The estimated Γ_c values were then corrected by subtracting the baseline, plotted against incubation time, and fitted to the percolation scaling law function (Equation 2).

$$P_\infty = K\,(p - p_c)^M \quad (2)$$

This equation is equivalent to the three-parameter power Belehradek function (OriginLab, Northampton, MA), where P_∞ is the calculated evolution of the correlation coefficient Γ_c over time, K is a proportionality constant, t is time, M is the universal percolation exponent, and p_c becomes $t_{gel\text{-}DLS}$, *i.e*. the critical gelation time at which the response diverges from that in the sol state [46]. The use of the Belehradek function to approximate percolation phenomena has been described [47–49].

The evolution of the viscoelastic properties for the CS:GNP mix (ratio 0.06:1) was further examined by small deformation oscillatory rheology using a stress-controlled rheometer Kinexus Ultra (Malvern Panalytical Ltd, UK) fitted with a truncated cone and plate geometry (gap 0.07 mm; diameter 50 mm). To this end, the CS/GNP mixture was prepared by mixing the corresponding amounts of CS and GNP stock solutions in a glass vial and incubated at 37 ºC in quiescent conditions during 18 h. A 1.5 mL aliquot of the mixture was loaded to the plate of the rheometer and the rim of the cone was covered with low viscosity silicon oil to avoid evaporation. The critical rheological gel point was defined as the crossover point of the elastic (G') and viscous (G'') moduli (ω= 6.28 rad/s), recorded at strain values, γ = 1 % over a period of up to 106 min), in line with previous studies [50,51].

Preparation of PC-NPs

The GNP-pre-crosslinked CS-TPP nanoparticles (PC-NPs) were prepared according to the general ionotropic gelation protocol described by Calvo *et al.* [6] with some modifications. First, GNP-pre-crosslinked CS was prepared at a GNP:CS mass ratio of 0.06:1, as explained above. To assess the optimal formulation to obtain PC-NPs of an average size ~200 nm and low polydispersity index or PdI (PdI ~0.1), different CS:TPP mass ratios were screened. To do this, GNP-pre-crosslinked CS was sub-diluted with 85 mM NaCl to reach CS concentrations ranging from 1-2 mg/mL. Similarly, TPP was also prepared in 85 mM NaCl, achieving final

concentrations ranging from 0.5-0.83 mg/mL. Aliquots of the two components were mixed in a 96-well micro plate in order to obtain PC-NPs with CS:TPP mass ratios ranging from 1.60:1 to 9.00:1 (see Table S1).

Two PC-NP prototypes of optimal size and PdI, namely PC-A, PC-B, with CS:TPP mass ratios of 3.5:1 and 2.6:1, respectively, were prepared by upscaling the preparation technique. Briefly, 1.875 mL (PC-A) or 2.250 mL (PC-B) of a TPP solution (0.63 mg/mL in 85 mM NaCl) were poured onto 4.125 mL (PC-A) or 3.750 mL (PC-B) of GNP-pre-crosslinked CS (sub-diluted to a CS concentration of 1 mg/mL with 85 mM NaCl) under magnetic stirring (500 rpm). When necessary, PC-NPs were isolated by centrifugation (40 min at 10000 x g and at 25 °C) in 1.5 mL vials containing a glycerol bed [52] and the pellets were re-suspended in 100 µL of water.

Physicochemical characterization of PC-NPs

The size distribution of NPs resuspended in Milli-Q® water was determined by DLS-NIBS. All measurements were performed in water at 25.0 ± 0.2 ºC and pH 6.36 . The ξ potential was determined by phase analysis light scattering with mixed mode measurements (M3-PALS) in the same instrument as for DLS-NIBS measurements and the determination was conducted by diluting (1:50) the PC-NPs in 1mM KCl (pH 6.36).

Determination of the PC-NP production yield and concentration

Batch PC-NP production yield was determined by centrifugation (40 min at 10000 x g and at 25 °C) of fixed volumes of freshly prepared PC-NPs in the absence of glycerol. After discarding the supernatants, the pellets were subjected to freeze-drying and the dry weight of the pellets was registered. The production yield was determined as follows (Equation 3):

$$Production\ yield\ (\%) = 100 \times \frac{m_{pellet} - m_{NaCl\,(pellet)}}{m_{total} \times V} \quad (3)$$

where: m_{pellet} is the dried mass of the pellet, $m_{NaCl\ (pellet)}$ is a corrective term that accounts for the mass of the residual NaCl present in the pellet (estimated as 0.075 mg NaCl in a 20-µL pellet), V is the volume used for freeze-drying (4.5 mL) and m_{total} is the total mass of the PC-NP components (GNP-pre-crosslinked CS and TPP) in the batch, as expressed in Equation 4:

$$m_{total} = \frac{C_{CS} \times V_{CS} + C_{TPP} \times V_{TPP}}{V_{batch}} \quad (4)$$

where: C_{cs} is the concentration of CS in the GNP-pre-crosslinked CS gel (1 mg/mL), V_{cs} is the volume of the GNP-pre-crosslinked CS gel used for PC-NP preparation (4.125 mL or 3.750 mL in PC-A and PC-B, respectively), C_{TPP} is the concentration of the TPP solution (0.63 mg/mL), V_{TPP} is the volume of the TPP solution used for PC-NP preparation (1.875 mL or 2.250 mL in PC-A and PC-B, respectively) and V_{batch} is the total volume of the PC-NP batch (6 mL). Thus, m_{total} was estimated as 0.93 mg and 0.90 mg for PC-A and PC-B, respectively. PC-NP concentration was calculated during subsequent experimental steps (*e.g.*, isolation, dilution, etc) by applying the corresponding concentration factor, f_c (*i.e.*, volume of PC-NPs for isolation or dilution relative to batch volume), as follows (Equation 5):

$$[NP]\left({}^{mg}/_{mL}\right) = m_{total} \times Production\ yield \times 10^{-2} \times f_c \quad (5)$$

Product yield determination was performed in triplicate.

Stability of PC-NPs in supplemented M9 minimal medium

60-µL aliquots of the isolated PC-NPs (PC-A and PC-B) were diluted in M9 minimal medium supplemented with 0.5% casamino acids, 1 mM thiamine hydrochloride and ampicillin (200 µg/mL), in a volume of 1 mL (final dilution = 1:17) and at a final concentration of ~0.15 mg/mL. The pH of the medium was 6.9 ± 0.05. The PC-NPs were incubated for 335 min in M9 minimal medium at 37 ºC under shaking (100 rpm) and size variation was monitored every ten minutes by DLS-NIBS at 37 ºC.

206 Bacterial strains and culture conditions

207 The *E. coli* strain Top10 was transformed with plasmid pSB1A3-BBa_T9002, carrying the
208 BBa_T9002 genetic device (Registry of Standard Biological Parts:
209 http://parts.igem.org/Part:BBa_T9002), kindly donated by Prof. John C. Anderson (UC
210 Berkeley, USA). The transformed strain is a biosensor that can respond to AHL[53].

211 Bacterial seeding and monitoring of culture´s fluorescence intensity (FI) and optical density
212 (OD_{600}) was performed as described in [42].

213

214 Evaluation of the ability of the PC-NPs to inhibit the QS response in a fluorescent *E. coli*
215 biosensor of AHL-mediated QS

216 The QS inhibitory activity of the PC-NPs was evaluated in terms of their ability to decrease
217 the AHL-mediated fluorescence response of the *E. coli* biosensor. Isolated PC-A and PC-B were
218 serially diluted in water. Ten-µL aliquots of these dilutions were pre-mixed with 180 µL of the
219 biosensor's culture and incubated for 1h at 37°C with shaking (100 rpm) in a flat-bottom, 96-
220 well plate. Blank (medium only) and control wells were inoculated with 10 µL of water and
221 incubated under the same conditions. After 1 h, 10 µL of $5x10^{-9}$ M AHL were added to the wells
222 to a final AHL concentration of $2.5x10^{-10}$ M and incubated for 300 min in the microplate reader
223 as explained above. Final PC-NP concentration in the plate ranged from 0.1 to 0.001 mg/mL.

224 Statistical comparison between PC-NP doses *vs*. controls were made with GraphPad Prism
225 version 6.00 (GraphPad Software, La Jolla California USA) using one-way ANOVA with
226 multiple comparisons Dunnett's Test (** $p \leq 0.01$; *** $p \leq 0.001$; **** $p \leq 0.0001$). For each
227 experiment, fluorescence intensity (FI) and OD_{600} were corrected by subtracting the values of
228 absorbance and fluorescence background and expressed as the average of three biological
229 replicates. FI was normalized to cell density (FI/OD_{600}), as described elsewhere [42,54,55]

230 Microscopy

231 Fluorescent imaging of the *E. coli* biosensor in the presence of AHL and PC-NPs was
232 performed as follows. 180-µL aliquots of the biosensor´s cultures were pre-incubated with 10-
233 µL aliquots of PC-NPs, to a final NP concentration of 123 µg/mL for 40 min at 37°C under
234 shaking (100 rpm) in capped vials. The PC-NP pre-treated biosensor was then induced with 10
235 µL of $5x10^{-9}$ M AHL. The cultures were then transferred to CytoCapture imaging dishes with
236 20-µm hexagonal cavities (Zell-Kontakt GmbH, Nörten-Hardenberg, Germany), and incubated
237 for a further 60 min at room temperature before imaging by confocal laser scanning microscopy
238 (CLSM). Imaging went on for a further 70 min. Control cultures were prepared by adding equal
239 aliquots of water instead of PC-NPs.

240 CLSM was performed using a Leica TCS SP2 spectral confocal scanner mounted on a Leica
241 DM IRES inverted microscope. Images were acquired under the following settings: an HCX PL
242 APO 63.0x 1.20 W CORR UV water-immersion objective, an argon excitation laser (488 nm),
243 a 134.1 µm pinhole (1.0 Airy unit), standard Leica settings for GFP beam path, an emission
244 bandwidth set to 500-600 nm, and a voxel width and height of 51.0 nm. Images were acquired
245 from single scans with a line average of 4.0, scan speed of 400 Hz, and 8-bit resolution. Image
246 processing was performed with Leica LAS AF Lite software. In every image, contrast and
247 brightness values were set to -63 and 0, respectively. To quantify fluorescence intensity data
248 from representative CLSM images, a number of regions of interest (ROIs) were drawn as lines
249 spanning the length of a representative number of cells (l =1.9-4.3 µm) and used to measure
250 pixel intensity across the cell. Every analysis included 3-7 images with 18-38 ROIs each. 3-
251 dimensional analysis of the culture was performed by collecting optical sections spanning a total
252 thickness of 7-8 µm, z-series. A total of 22-27 frames were collected in each section with 0.3-
253 µm gaps between frames. Statistical comparison between PC-NP doses *vs.* controls were made

with GraphPad Prism version 6.00 (GraphPad Software, La Jolla California USA) umpaired t-test (**** $p \leq 0.0001$).

RESULTS

Chemical co-crosslinking of CS with GNP

Prior to the preparation of PC-NPs, pre-crosslinked CS/GNP mixtures with optimized composition and rheological properties were prepared in 85 mM NaCl after screening various GNP:CS mass ratios (see Materials and Methods). Figure 1A shows representative images of GNP-pre-crosslinked CS at GNP:CS mass ratios of 0.06:1, 0.12:1 and 0.24:1 after 72 h incubation at 37˚C under shaking. Of note, is the formation of a dark blue color stemming from secondary products of the reaction between CS and GNP [13,15]. As expected, both color intensity and the apparent loss in fluidity increased with increasing GNP:CS mass ratios [13]. At the highest GNP:CS mass ratio, a gel-like consistency was visually apparent (0.24:1 GNP:CS mass ratio in Figure 1A). The kinetics of the crosslinking reaction were monitored by UV/VIS, DLS-NIBS and small deformation rheology. Figure 1B shows the UV/VIS spectra (λ = 200-900 nm) depicting the time-course evolution of the GNP crosslinking reaction for CS/GNP mixtures with a GNP:CS mass ratio of 0.06:1. As previously reported, a characteristic peak between 280-300 nm (dotted line in Figure 1B), increases concomitantly with the progression of the GNP crosslinking reaction [20]. The inset in Figure 1B represents the evolution of the peak at 280 nm over time. The height of the peak increases steeply during the first 80 h of incubation and reaches a plateau at later times. This evidence made us conclude that the covalent crosslinking reaction was completed after 80 h. Previous studies addressing the evolution of the crosslinking reaction between chitosan and genipin [14], have also used UV together with FTIR and ^{1}H NMR spectroscopy and unequivocally accounted for the chemical reaction at play.

To determine the critical gel time ($t_{gel\text{-}DLS}$) the DLS-NIBS intensity correlation data at different reaction times were fitted to the KWW-based stretched exponential function (Eq. 1, see Materials and Methods), as previously described [45,51]. The values of the derived relaxation rate parameter (Γ_c) were then fitted to the percolation function (Eq. 2, see Materials and Methods) to estimate $t_{gel\text{-}DLS}$ [44]. Figure 1C shows the DLS-derived correlograms, expressed as correlation coefficients *vs.* delay times for a GNP:CS mass ratio of 0.06:1 and at different incubation times. The inset shows a representative correlogram of this GNP:CS mixture after 0.6 h incubation. The best-fit of the experimental data to the KWW-based stretched exponential function is represented by a solid line.

Noticeable from Figure 1C is the reduction in the magnitude of the intensity correlation coefficients at early delay times as incubation time increases. Figure 1D plots the area under the curve (AUC) from the correlograms of Figure 1C at different incubation times. The monotonic decay of the magnitude of AUC with incubation time is depicted by a solid line in Figure 1D. The strong decay in the initial amplitude of the correlation intensity, as depicted in Figure 1D, has been proposed as a good indicator of the critical gelation time in previous studies with similar soft systems [45,56]. Further analysis shows that correlating the KWW-derived parameters with delay time is consistent with a sol-gel transition resulting from the chemical crosslinking reaction. These changes include the enlargement of CS macromolecular dimensions at early times, the increase in crosslinking density, and the loss of ergodicity at longer times [45]. Figure 1E shows a plot of the estimated Γ_c, as extracted from the fits of the correlograms, to the KWW-based stretched exponential function shown in Figure 1C. The values of Γ_c remained noisy around a baseline during the first ~35-500 min of incubation. After this phase, a sharp increase of Γ_c values is observed ("take-off phase", from ~500-3000 min) that levels off late in the reaction ("plateau phase", after ~3000 min). This profile correlates closely with the one

described by de Morais *et al*. [45] for the chemical crosslinking of chitosan with glutaraldehyde. As explained by these authors, the relaxation rate Γ_c, decreases at earlier reaction times due to an increase in viscous, hydrodynamic interactions between macromolecular CS coils and the solvent that result in longer macromolecular CS coils. At longer reaction times, further intermolecular crosslinking results in a decrease of the dimensions of the macromolecular coils in the gel structure, thus explaining the sharp Γ_c increase [45]. Upon closer inspection, the profile of Γ_c *vs.* reaction time in Figure 1E closely resembles the kinetics of a classical percolation process. In fact, the behaviour of gels at the sol-gel phase transition has been extensively described in terms of Percolation Theory (PT) [44]. Percolative gelation involves a sharp transition at some intermediate critical point ($p = p_c$, Eq. 2; see Materials and Methods), where an infinite cluster starts to appear: a gel for p above p_c [44]. This critical point, or gel point, $p = p_c$ becomes $t = t_{gel\text{-}DLS}$ in our system and determines the critical gelation time (see Materials and Methods). We fitted the Γ_c values between the "take-off phase" and the "plateau phase" to the three-parameter power Belehradek function [47,48]. From this percolation fit, depicted by a solid line in Figure 1E, a $t_{gel\text{-}DLS}$ of 640.7 min and an M exponent of 0.29, were obtained. The value of the M is not too far from the universal exponent reported for a 3D classical percolation process, M = 0.45 [44]. From these results, we can infer that a gel-like state is achieved after 10.7 h of incubation of the GNP-CS mixture at 37˚C and at a GNP:CS mass ratio of 0.06:1.

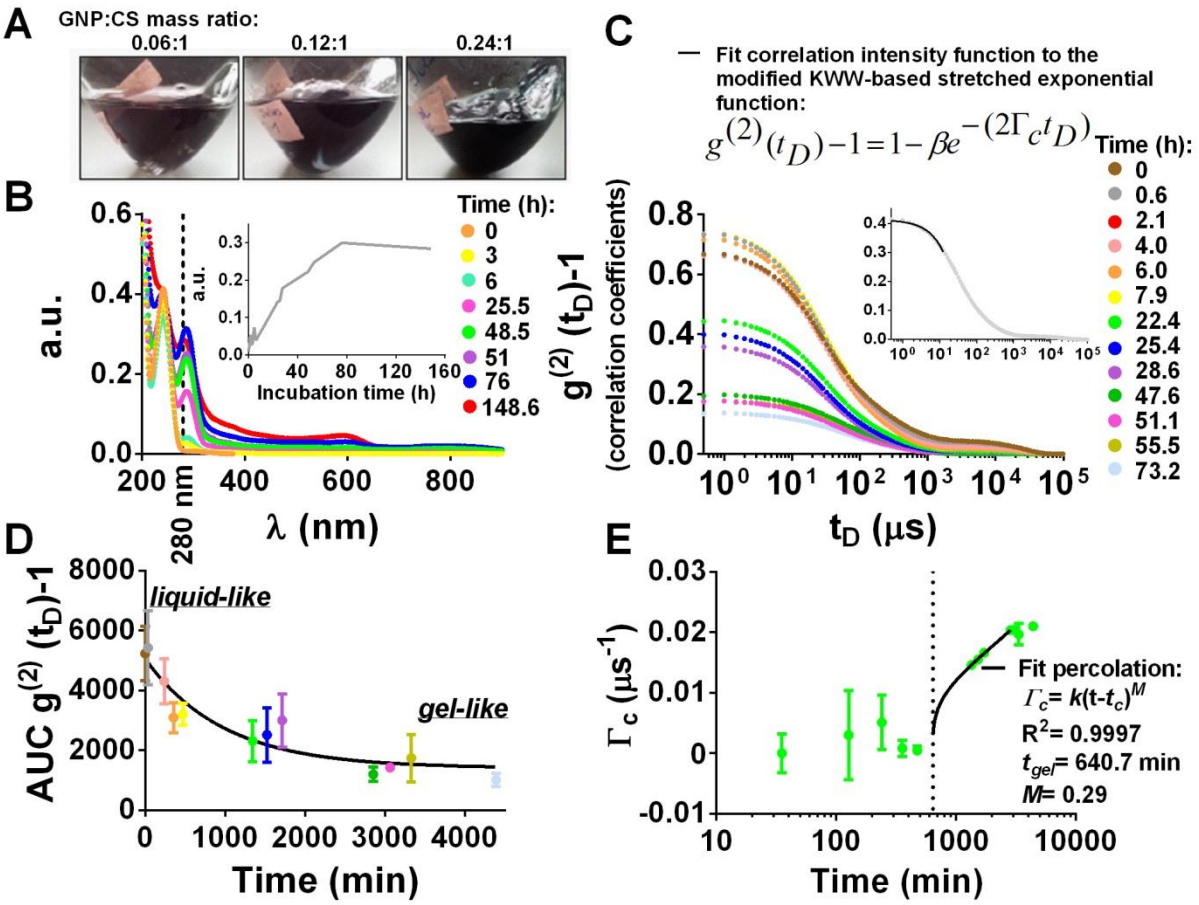

Figure 1. Monitoring chemical crosslinking of CS with GNP over time. A. Representative snapshots of the gelation-like process after 72 incubation at 37˚C with shaking. The images show the formation of blue color as a secondary product of the reaction of CS and GNP at different GNP:CS mass ratios; namely 0.06:1; 0.12:1 and 0.24:1. B. Time-course evolution of the crosslinking reaction for CS/GNP mixtures at a GNP:CS mass ratio of 0.06:1, as monitored by UV-vis scanning (λ = 200-900 nm). Color key indicates reaction times (left). The dotted line indicates the characteristic peak of the CS/GNP gelation reaction at λ= 280 nm. The inset shows the magnitude variation of the characteristic peak (λ= 280 nm) over time. Data show single representative reaction. C. DLS-NIBS intensity correlograms at a GNP:CS mass ratio of 0.06:1. Color key indicates reaction times (left). The inset shows a representative plot at t= 73.2 h, where the solid black line represents the best-fit to the KWW-based stretched exponential function at early delay times. D. Evolution of the AUC from the plots in C with reaction time. Color-coded as in C. The solid line represents the best-fit of the data to the one-phase decay function (GraphPad Software, La Jolla California USA). E. Evolution of the relaxation rate Γ_c, as estimated from the fits of the correlograms shown in C to the KWW-based function at different reaction times. The solid line corresponds to the best-fit of the data to the percolation function (Equation 2, see Materials and Methods). The dotted line shows the estimated critical time of gelation ($t_{gel\text{-}DLS}$) at ~640.7 min.

To further confirm the formation of a gel network in rheological terms resulting from the sol-gel transition of the GNP/CS mixture of GNP:CS mass ratio 0.06:1, we examined the evolution of the viscoelastic properties using small deformation oscillatory rheology. The results (Figure S1) revealed that an incipient gel network is formed at a rheological critical gel time ($t_{gel\text{-}rheo}$) of ~1118 min. This is evident from the crossover of the G' and G'' moduli, and the drop in tan δ. Also, a frequency sweep recorded after 1200 min, revealed all the hallmarks of a gel network (i.e., G' > G'') and dependence of η* on the frequency with a slope of ~ -1.0 (Figure S2). Despite being at the limit of sensitivity of the rheometer, these determinations provide unequivocal evidence of the sol-gel transition of the system. It should be noted, however, that the magnitude of the critical gel time obtained by DLS-NIBS ($t_{gel\text{-}DLS}$ ~640.7 min) was ~2-fold lower than that determined by small deformation rheology ($t_{gel\text{-}rheo}$ ~1118 min). The apparent large discrepancy between the two determined values could be the result of the different experimental resolution capacity of each technique, as we have shown in a previous study at low chitosan concentrations (< 2 mg/mL) [51]. Indeed, we have been able to show that within experimental error, DLS-NIBS, microviscosimetry, and small deformation rheology, constitute robust methods to determine the critical sol-gel transition of CS-based systems [51].

Optimization of PC-NP size and polydispersity

To obtain PC-NPs, the GNP-pre-crosslinked CS mixtures, formed as explained above, were further crosslinked with the ionic crosslinker TPP by following the classical ionotropic gelation protocol [6]. To rapidly assess the composition of PC-NPs with the lowest average NP diameter and PdI, we followed the classification method described by Calvo et al and Dmour & Taha [6,57]. In addition, based on our previous work and on the work of others [5,42,58–60], we used 85 mM NaCl as solvent instead of water to better modulate the size and the polydispersity of PC-NPs

362 over a range of CS:TPP mass ratios. It has been suggested that the addition of a low amount of
363 monovalent ions to CS NP suspensions aids in the optimization of the hydrodynamic radius and
364 screens the electrostatic repulsion of the charged amino groups in CS, thus adopting a more
365 compact conformation increased flexibility and colloidal stability, and lower polydispersity [5,58].
366 Low average diameters and PdI values were achieved with CS:TPP mass ratios in the range
367 of 1.60:1 to 9.0:1 (See Materials and Methods and Table S1). Figures 2A and 2B show the
368 dependence of the size and PdI of PC-NPs on the relative TPP and CS concentrations,
369 respectively. In both cases, regions with colours ranging from green to red can be interpreted as
370 hills with high size (Figure 2A) or high PdI values (Figure 2B), whereas regions with colors
371 ranging from purple to blue correspond to valleys with sub-micron sizes and low to medium PdI
372 values. Figure 2A shows that it is possible to obtain PC-NPs with Z-average diameter between
373 ~200 and ~300 nm by using CS concentrations ranging from 0.5 to 1.5 mg/mL and TPP
374 concentrations below 0.2 mg/mL. Close inspection of the contour plot also shows three
375 conspicuous regions with sizes above ~600 nm, which correspond to specific compositions of
376 CS and TPP, namely region 1, ≤0.9 mg/mL CS and ≥0.25 mg/mL TPP; region 2, 0.9-1.1 mg/mL
377 CS and ~0.3-0.4 mg/mL TPP; and region 3, ≥1.1 mg/mL CS and >0.3 mg/mL TPP (white dotted
378 lines in Figure 1A). Figure 2B shows that low polydispersity was achieved in the PdI range of
379 0.2-0.3 for CS concentrations of 0.5-1.5 mg/mL and TPP concentrations below 0.2 mg/mL.
380 Similarly to Figure 2A, the contour plot in Figure 2B displays two main regions of high
381 polydispersity, PdI between ~0.5-1, which correspond to the following CS and TPP
382 combinations: region 1, ≤0.7 mg/mL CS and ≥0.25 mg/mL TPP and region 2, ~0.7-1.1 mg/mL
383 CS and >0.35 mg/mL TPP (white dotted lines in Figure 1B). Figures 2C and 2D summarize the
384 dependence of the size and PdI, respectively, on CS:TPP mass ratios. The Figures show that it
385 was possible to obtain PC-NPs with an average diameter ranging from 100-250 nm and a low

PdI values, ~0.1-0.2, under a wide range of CS:TPP mass ratios (2.6:1 to 9:1). PC-NPs could be easily dispersed in water, as has been reported for NPs prepared from CS of similar DA [61,62]. Two PC-NP prototypes displaying optimal size and PdI (indicated by black circles in Figures 2C and 2D) were obtained with CS:TPP mass ratios of 3.5:1 and 2.6:1, respectively. These prototypes were designated as PC-A and PC-B and were selected for further studies.

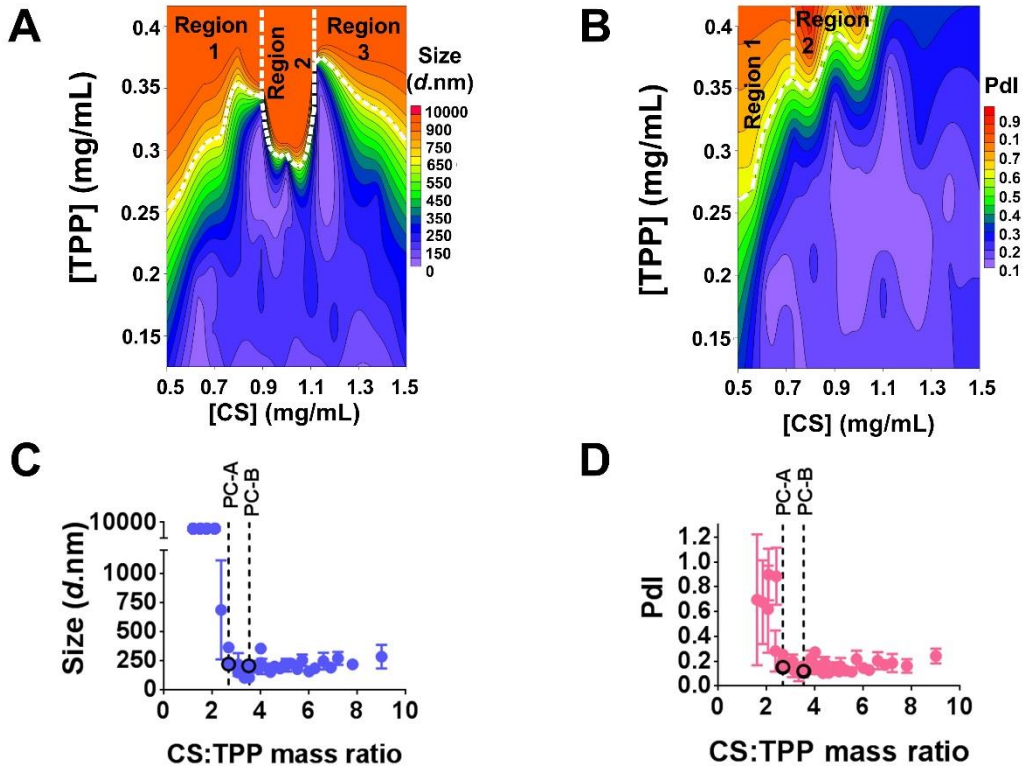

Figure 2. Dependence of the size and PdI of PC-NPs on CS:TPP mass ratio. A and B. Contour plots showing the dependence of the size (A) and PdI (B) of PC-NPs on the CS and TPP concentrations. [CS] = 0.5 - 1.5 mg/mL; [TPP] = 0.1-0.4 mg/mL; CS:GNP mass ratio = 1:0.06. White dotted lines in panels A and B show representative size and PdI regions (see text). C and D. Variation of PC-NP size (C) and polydispersity (D) as a function of the chitosan:TPP mass ratio. Dotted lines show the CS:TPP mass ratios 2.6:1 and 3.5:1, which correspond to the PC-NP prototypes PC-A and PC-B (black circles), respectively. Data represent the mean and standard deviation of three replicates. All measurements were conducted in water at 25±0.2 ºC.

The PC-A and PC-B prototype formulations were prepared by upscaling the PC-NP preparation method to 10-mL batches with a production yield, of 44.5 and 40.9%, respectively (see Materials and Methods). The physicochemical characteristics of the PC-NP batches were analyzed by DLS-NIBS both before and after isolation (see Materials and Methods). Figure 3 shows the polydispersity and the average diameter of PC-A (Figure 3A) and PC-B (Figure 3B), before and after their isolation (cyan and orange plots, respectively). As shown in Figure 3A, PC-A underwent a reduction in PdI after isolation, going from ~0.1 to ~0.04 (upper left y-axis). Yet, the average diameter remained stable (average diameter = 123.4 ± 6.6 nm and 124.0 ± 4.0 nm, for the non-isolated parent batch and the isolated batch, respectively). The bottom panels in Figure 3A show a slight reduction in the width of the size distribution for isolated PC-NPs, relative to their parent batch. As shown in Figure 3B, the parent batch of non-isolated PC-B is characterized by a lower PdI than that of PC-A, with a slight Pdl increase after isolation, namely from ~0.02 to ~0.04 (upper right y-axis). Parent PC-B NPs are, on the other hand, slightly bigger in size than their PC-A counterparts, with an average diameter of 140.8 ± 3.2 nm before and 128.7 ± 2.5 nm after isolation. The bottom panels in Figure 3B reveal no important differences between the size distributions of parent and isolated PC-B batches. As expected, both PC-A and PC-B showed a marked positive ξ potential, of ~+33 mV (data not shown), which is consistent with the presence of charged amine groups from CS exposed to the PC-NP surface [63,64].

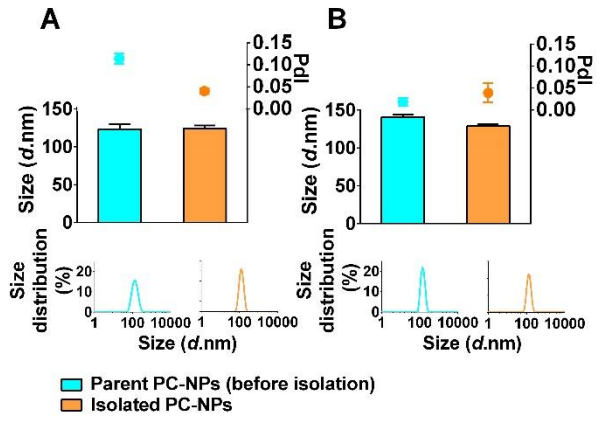

Figure 3. Physico-chemical characterization of PC-NPs. A and B. Size and polydispersity of the parent batch before (cyan) and after (orange) isolation of PC-A (A) and PC-B (B) NPs. Bars represent mean size (left y-axis), whereas dots represent PdI values (upper right y-axis). Bottom panels show representative DLS-NIBS size distribution plots for both PC-NP prototypes before and after isolation.

PC-NP stability in M9 minimal medium

To evaluate the physical stability of PC-NPs designed for microbiological assays, we monitored particle size evolution during PC-NP incubation in our bioassay medium (see Materials and Methods). The chosen time range of these experiments, 335 min, was not arbitrary, as it spanned the duration of our typical bioassays with the *E. coli* biosensor (see below). Size and polydispersity plots in Figure 4 revealed that both PC-A (Figure 4A) and PC-B (Figure 4B) remain fully stable during incubation in microbiological medium. The low PdI values between 0.06-0.1 confirmed that no aggregation or particle-growth took place during the incubation. Figures 4C and 4D show that DLS-NIBS size distributions remained changeless over time in both cases.

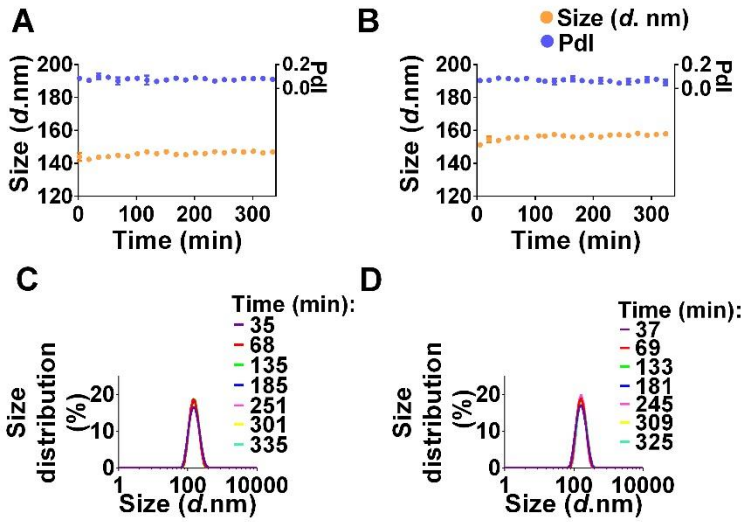

Figure 4. Stability of PC-NPs in bioassay medium. A and B. Variation in size (orange dots; left y-axis) and in PdI values (blue dots; right y-axis) of PC-A (A) and PC-B (B) upon incubation at 37 °C in bioassay medium. C and D. Representative DLS-NIBS size distributions of PC-A (A) and PC-B (B) at different times of incubation.

Evaluation of the quorum quenching activity of PC-NPs using a fluorescence *E.coli* biosensor

To analyze the QQ activity of PC-NPs, we used an *E.coli* biosensor that displays GFP fluorescence in response to external AHL [42,53]. When endpoint measurements are considered, both PC-A (Figure 5A) and PC-B (Figure 5B) promoted a significant reduction in the normalized fluorescence response of the biosensor, FI/OD_{600}. Comparison of Figures 5A and 5B indicates that PC-B is slightly more active than PC-A, with relative reductions of end-point FI/OD_{600} in the ranges of ~50-92% and ~35-85% of the control intensity, respectively. The end-point measurements show the lack of a clear dose-dependent reduction of the response. Figures 5C and 5D show the effect of PC-A and PC-B treatments, on the growth rate of the *E. coli* biosensor (see also Figure S3). Both PC-NP prototypes promote a significant reduction in growth rate that, much like the reduction in normalized fluorescence, is not proportional to the administered dose. Comparing Figures 5A and 5B to 5C and 5D shows that the magnitude of

457 the growth impairment exerted by PC-NPs is much smaller than their effect on normalized
458 fluorescence.
459
460 The plots shown in Figures 5A-D fail to reveal the dynamics of the effect of PC-NPs on the
461 growth and response of the biosensor. While we saw a significant degree of variation from
462 experiment to experiment, careful inspection of the average FI/OD_{600} traces (Figures 5E and 5F,
463 see also Figures S4-S6), yields the following conclusions. First, in the absence of PC-NPs the
464 biosensor displays a biphasic response with clear initial burst of fluorescence (see red-framed
465 area "1" in inset in Figure 5E and also Figures 5F, S4-S6). Following this initial burst, the control
466 response steadily grows reaching a maximum of fluorescence at about ~250 min (see red-framed
467 area "2" in inset in Figure 5E and also Figures 5F, S4-S6). The burst was followed by a phase
468 of fluorescence dilution at most of the PC-NP concentrations tested (black star in Figures 5E
469 and 5F). At low PC-NP concentrations a recovery phase is sometimes visible (horizontal arrow
470 in Figures 5E and 5F, but see also Figures S4-S6). Notably, CLSM imaging of the biosensor
471 was consistent with the notion that the PC-NP-dependent decrease in fluorescence was much
472 more accused than the antimicrobial effect (*cf*. Figure S7A and B). In the same assays, we also
473 observed cell aggregates in the presenec of the NPs (Figure S8), in agreement with previous
474 studies [42,65,66].
475 Figures 5G and 5H show the average OD_{600} traces during the initial 200 min of incubation
476 after AHL addition. Starting at a concentration of 13.75 µg/mL, incubation of the biosensor with
477 PC-NPs resulted in curves displaying "shoulders" (arrows in Figures 5G and 5H, Figure 6). To
478 better illustrate the nature of the PC-NP-induced "shoulders", in Figure 6 we show the individual
479 traces from all the three biological replicates, together with the average control trace. The boxes
480 in Figure 6 show that the "shoulders" observed in the average OD_{600} traces are related to the

existence of PC-NP-dependent anomalies in the OD_{600} readings at certain times during growth (Figures 6C-F see also Figure S4). While there existed a significant degree of experiment-to-experiment variation regarding the magnitude of the anomalies in the growth kinetics of the PC-NP-treated cultures, the dose-dependence in the timing of the anomalies was very reproducible (Figure 6; see also Figure S4-S6). This dose depencence is more clearly illustrated in Figure 7, which shows the relationship between the time of onset of OD_{600} anomalies and the concentration of PC-NPs. Strikingly, the data for both PC-A and PC-B can be easily fitted to hyperbolic curves, typical of dose-response relationships. The slightly steeper curve of PC-B is consistent with the higher inhibition of FI/OD_{600} displayed by these NPs in endpoint QQ measurements (*cf.* Figure 5A and 5B)

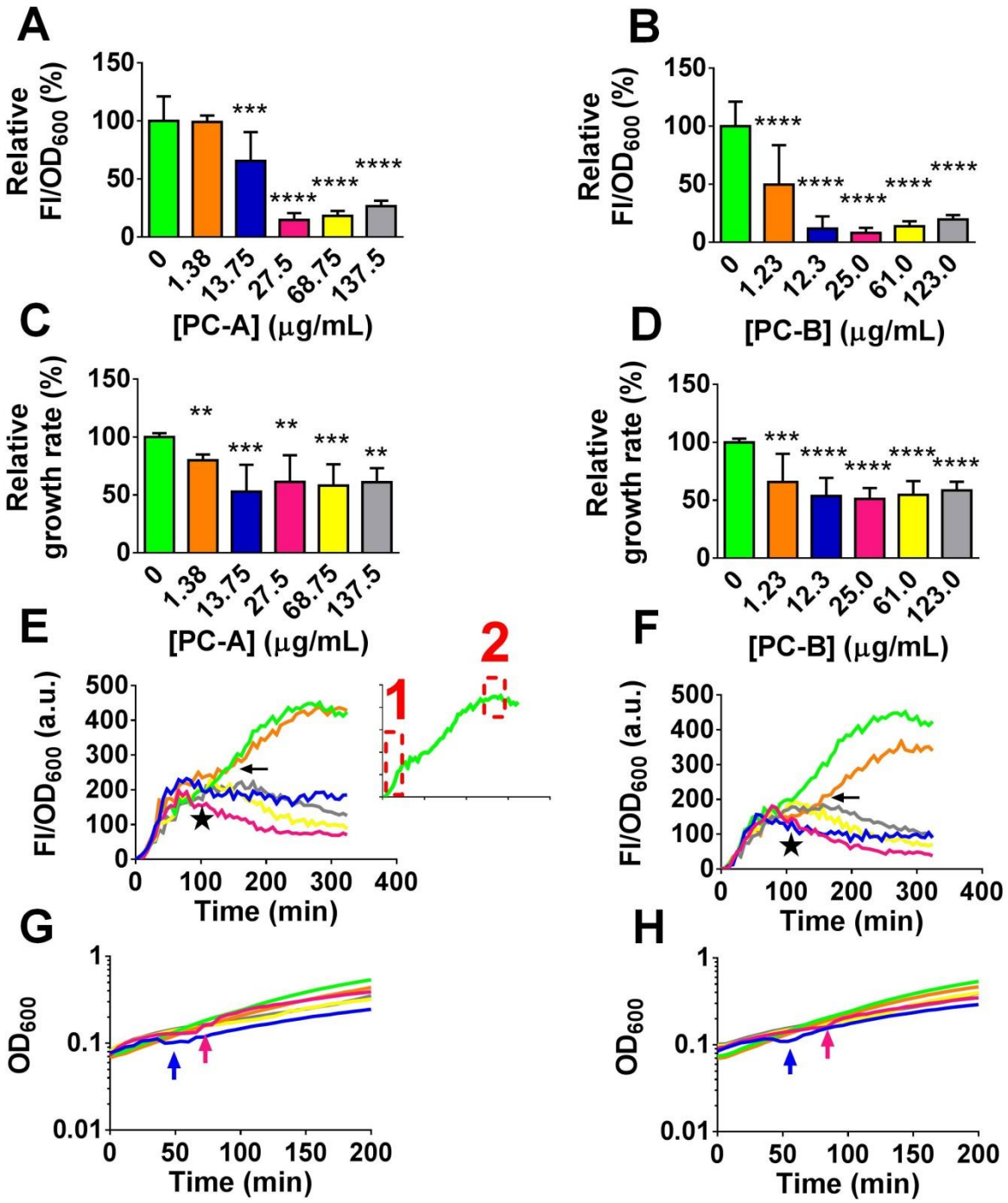

Figure 5. Effect of PC-NPs on the QS-based fluorescent response and the growth of the *E. coli* biosensor. A and B. Endpoint FI/OD_{600} responses of the biosensor after treatment with various doses of PC-A (A) and PC-B (B) for 60 min prior to the addition of AHL. Data represent the mean and standard deviation of two independent experiments with three biological replicates each. P values are indicated as follows:

**, $p \leq 0.01$; ***, $p \leq 0.001$; ****, $p \leq 0.0001$. C and D. Endpoint effect of PC-A (C) and PC-B (D) treatments on the bionsensor's growth rate. The mean and standard deviation of three independent experiments with three biological replicates each is shown. E and F. Representative FI/OD_{600} average traces of cultures treated with PC-A (E) and PC-B (F). The averages were obtained from a single experiment with three biological replicates. The traces are color coded as in A and B. For the sake of clarity, no error bars are shown (but see Figures S1 and S2). Inset in panel E shows the typical biphasic response of non-treated cells. Box "1", initial burst of fluorescence. Box "2", fluorescence maximum. Arrowheads indicate the fluorescence recovery phases described in the text. Stars in panels E and F show the fluorescence dilution phase described in the text. G and H. Average growth curves for biosensor cells pre-treated with PC-A (G) and PC-B (H) prior to the addition of AHL. Arrowheads indicate the PC-NP-induced "shoulders" described in the text. The traces represent the mean of a single experiment with three biological replicates and are colour coded as in E and F. For the sake of clarity, no error bars are shown (but see Figure S4). P values are indicated as follows: **, $p \leq 0.01$; ***, $p \leq 0.001$; ****, $p \leq 0.0001$.

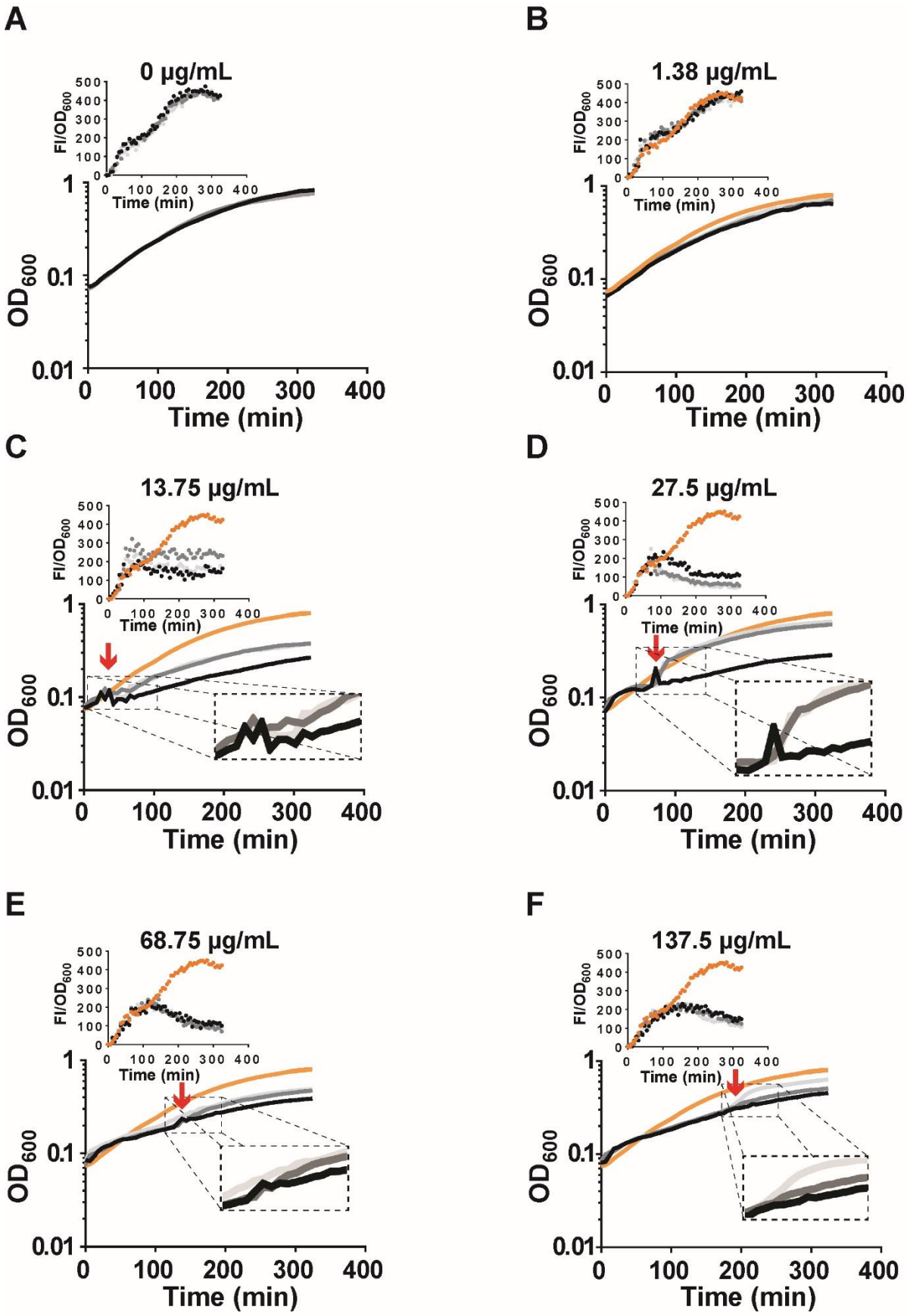
A
0 µg/mL
B
1.38 µg/mL
C
13.75 µg/mL
D
27.5 µg/mL
E
68.75 µg/mL
F
137.5 µg/mL
FI/OD600
Time (min)
OD600
0.01
0.1
1
0
100
200
300
400
500

512

Figure 6. Growth of the biosensor in the presence of increasing PC-A concentrations (A-F). The individual traces corresponding to the three replicates from a single experiment are shown with shades of gray. Orange traces: no NP controls. Boxes show enlarged views of the "shoulders". X axis: time in min. Y axis: OD_{600}. Insets show the corresponding plots of FI/OD_{600} *vs.* time for each treatment.

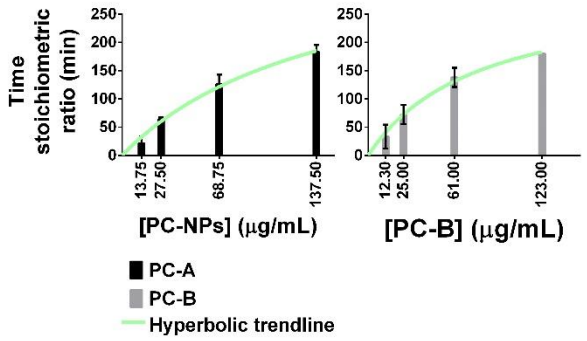

Figure 7. Dose dependence of the OD_{600} anomalies. The time (in min) needed to reach the "bumpy region" at increasing PC-NP concentrations is shown for PC-A (black bars) and PC-B (gray bars). The times were estimated from visual examination of the OD_{600} *vs.* time plots shown in Figures 6 and S2-4, considering that the "bumpy region" was reached once the individual traces diverged from one another (close-up boxes in Figures 6 and S4-6). Data represent the mean and standard deviation of two independent experiments with three replicates each. The green line shows the approximation of the data to a hyperbolic curve (GraphPad Prism version 6.0).

DISCUSSION

We recently reported that TPP-crosslinked NPs (ionically crosslinked; IC-NPs) displayed substantial QQ activity despite their inherent colloidal instability in microbiological medium [42]. We also showed that genipin-crosslinking of IC-NPs resulted in more stable NPs (co-crosslinked; CC-NPs), albeit with a substantial loss of their QQ activity. This has motivated us to explore novel strategies to improve the physicochemical properties of IC-NPs while maintaining their QQ activity. In the present work, we addressed a new method for the fabrication of TPP-crosslinked NPs in which the pre-crosslinking of CS with GNP was followed by NP formation by conventional ionotropic gelation in the presence of TPP.

The most surprising aspect of the observed data of our study is that when the pre-gelled GNP/CS mix (GNP:CS mass ratio 0.06:1.0) was further ionotropically crosslinked by controlled addition of TPP (over a wide CS:TPP mass ratio of 2.6:1 to 9:1), the system turned into nanoparticles of small conserved diameters (~100-150 nm) and low polydispersity (~0.1-0.2). To account for this phenomenon, we suggest the following. NP formation is the consequence of two separate physicochemical processes. Firstly, gelling by the formation of small nanoclusters resulting from the crosslinking of chitosan by GNP. Given the fact that the reaction was left to proceed to near equilibrium (72 h, Fig 1D), we can regard the gelling process to be under thermodynamic control [51]. The entropic cost of the loss of CS conformational mobility, as a result of the introduction of covalent "knots" between the polymer chains during the crosslinking process, is compensated by an overall gain in enthalpy due to the formation of new chemical bonds and the favourable solvation of $-NH_3^+$ groups preferentially oriented at the surface of the GNP-driven nanoclusters. As a result, a net decrease in surface free energy is obtained during gelling. Secondly, the addition of TPP to the incipiently gelled chitosan solution results in the shielding of the positively charged free amino groups in chitosan, leading to the condensation of the pre-gelled clusters into small discrete particles. The addition of TPP likely displaces the equilibrium and further contributes to the loss of polymer conformational mobility and to the entropically unfavourable, uneven partitioning of TPP within the CS-GNP pre-gelled clusters and the solvent. This would drive the system into phase segregation of the clusters, as recently argued [51]. However, the huge entropy loss due to the tendency of a limiting amount of TPP ions to partition into the chitosan phase, is counteracted by an overall reduction in particle size and consequent lower surface free energy, thus maintaining the system as a one-phase suspension. This is consistent with results observed in chitosan-dextran sulphate nanocomplexes, where decreasing the kinetic control of the particle formation while favouring a thermodynamically

(*i.e.* equilibrium) controlled process is required to achieve nanoparticles of high colloidal stability [67]. In summary, we assume that the process uncovered here to fabricate CC-NPs leads to the formation of dense small colloidal particles stabilized by the presence of surface positive charges and by conformationally "frozen" polymer loops, both of whichcontribute to electrostatic repulsion and steric stabilization of the system at the same time. A schematic view of the proposed model is shown in Figure 8.

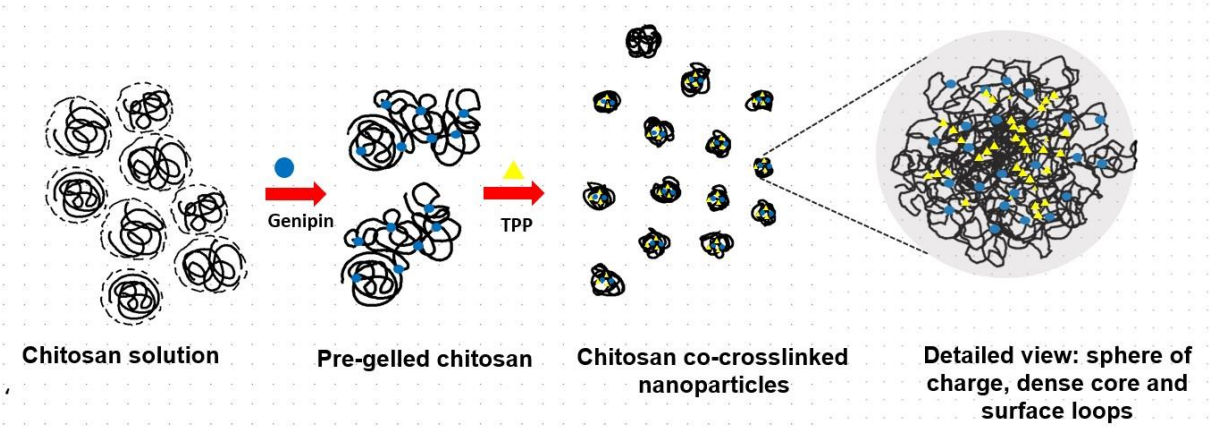

Figure 8. Model of formation of PC-NPs showing the two steps of crosslinking with genipin and TPP and details of the structure and surface topology of the furnished nanoparticles.

Even when the precise mechanism at play in the fabrication of PC-NPs remains to be fully elucidated, one practical implication of our new protocolwas to uncover a new, fabrication protocol of physico-chemically stable nanoparticles. When compared to our previous fabrication method [42], our new strategy offers a simplified and highly reproducible procedure to obtain PC-NPs with a satisfactory yield and improved physico-chemical properties such as size, ζ potential, and stability in biological medium (summarized in Table I) [42]. The resulting PC-NPs had overall

small diameter (~150 nm) and low PdI values (~0.1-0.3) from a wide range of relative CS:TPP mass ratios. Genipin pre-crosslinking also makes the fabrication protocol much more straightforward and reliable. Crucially, the new protocol reduces the centrifugation steps used to isolate NPs from non-crosslinked CS [42,52,68]. As a result, the reproducibility of the fabrication method was greatly improved. We believe that the improved characteristics of PC-NPs, relative to related NPs [42], are likely due to a minimization of TPP induced aggregation [58,60]. Future work and microscopic analysis should explore whether the two-step raspberry-like organization of NPs described by Huang and Lapitsky [58], proposed for the related CC-NPs [42] also applies to PC-NPs. On the same note, the possibility that PC-NPs may have a core-shell structure, as described for CC-NPs [42], should also be explored.

Table I. Physico-chemical characteristics of our CS-NPs (this work and [42]).

	IC-NPs [42]	CC-NPs [42]	PC-NPs
Size in water (*d*. nm)	617 ± 232	151 ± 8	124 ± 4
Size in M9 medium[(*)] (*d*. nm)	N/A [(*)]	226 ± 19	147 ± 1
ξ (mV)	+25 ± 6	+20 ± 2	+33 [(&)]
PdI	0.1-0.2	0.1-0.2	0.03-0.05
Production yield (%)	40 ± 8 [($)]	40 ± 8 [($)]	50 ± 1
QQ activity	high	moderate	high
Antimicrobial activity	yes	yes	yes
Cell-density dependent activity	N/A	N/A	yes
Fabrication steps	2	4	3

[(*)] After 6 h incubation in M9 minimal medium at 37 ºC.

[(&)] IC-NPs were unstable in M9 minimal medium at 37 ºC and there is no reliable DLS data available.

[($)] The measurement was performed only once.

601 (!) Production yield was estimated for the parent-non-isolated batch of IC-NPs before obtaining isolated IC- and
602 CC-NPs.

603

604 The notable stability of PC-NPs in bacterial culture medium (pH 6.9) coincides also with that
605 of core-shell CC-NPs, which also contain GNP and TPP but that underwent a different
606 fabrication process, leading to distinct properties (see below) [42]. This stability, we argue, is the
607 result of the combination of the covalent crosslinking and the ionotropic gelation used to
608 fabricate these nanoparticles, as explained above. Altogether, the furnished PC-NPs (and CC-
609 NPs) resist the tendency to disassemble and to inexorably aggregate that is observed with
610 classical chitosan nanoparticles (IC-NPs) in physiological media (pH ~7.0) [42,68]. Undoubtedly,
611 to be stable in bacterial medium is a major asset of PC-NPs, shared also by CC-NPs. .
612 We showed that PC-NPs display moderate antimicrobial activity, as judged by decreased OD_{600}
613 readings, and strongly interfere with the QS-based fluorescence activity of the *E. coli* biosensor
614 (Figures 5-6). Since the fluorescence measurements have been normalized to cell density
615 (FI/OD_{600}), the simple idea that the antimicrobial effect of our NPs might be responsible for the
616 fluorescence decrease does not hold. On the contrary, the results show that the decrease in
617 fluorescence was of greater magnitude than the OD_{600} drop caused by the antimicrobial effect.
618 Preliminary CLSM trials confirmed the existence of a drastic decrease in per-cell fluorescence
619 at the single-cell level (*cf.* Figure S7A and S7B and Figure S7C and S7D) that was not
620 accompanied by a parallel decrease in cell numbers (Figure S7E). This is in good agreement
621 with the idea that the decreased OD_{600} values and reduced fluorescence are separate effects of
622 PC-NP treatment. Indeed, it is even possible that the mangnitude of the antimicrobial effect is
623 an artifact coused by PC-NP-induced bacterial aggregation, as suggested earlier [42]. We have
624 previously shown that addition of CS NPs and nanocapsules (NCs) to bacterial cultures often

results in growth anomalies such as those observed here (Figure 6) [42,65]. In the case of CS NCs, we were able to show that only a limited number of NCs could electrostatically bind per bacterial cell, leading to the concept of the *stoichiometric ratio* (SR) of NC/bacterium [42,65]. At this NC/bacterium ratio, the negative ζ-potential potential of the bacterial envelope is counteracted by the positive charge of the NPs [65]. Increasing the NC concentration beyond the SR resulted in no further NP binding [65]. We have showed that the SR is accompanied by maximal, NC-induced cell aggregation [65]. Here, we have presented direct evidence showing bacterial aggregation in the presence of PC-NPs (Figure S8), further lending support to the hypothesis that our OD_{600} readings might not accurately reflect the actual cell density of the treated cultures. We believe that the OD_{600} growth anomalies in the form of "shoulders", observed in the presence of intermediate concentrations of PC-NPs (Figures 5G and 5H, Figure 6, and Figures S4-6), are likely related to cell aggregation and to the concept of SR, as described by Qin *et al*. [65]. This interpretation would shed some light on the conspicuous lack of dose dependence during PC-NPs treatment of biosensor cells, that was already noted in our previous work [42] and that is clearly illustrated in the endpoint results of Figure 5 [65]. Here, we have further investigated these growth anomalies, by timing their onset at different NP concentrations. When this was done, dose dependence relative to NP concentration became clearly apparent, as shown in Figure 7. While we have observed important levels of experimental variation (see Figure 6 and Figures S4-6), a trend is clearly evident in which "shoulder" formation accurs at longer times as NP concentration increases. To explain this dose dependence at the onset of the growth anomalies, we will return to the SR concept. Since at constant NP concentrations, growing bacteria will find themselves at decreasing NP/bacterium ratios [65], we reasoned that PC-NP-induced aggregates produced at NP/bacterium ratios higher than the SR (early during growth) would be disrupted as these ratios became smaller than the SR. The dependence of the SR on cell density,

649 together with its potential involvement in the appearance of OD_{600} anomalies implies that the
650 time at which a growing bacterial population encounters its SR must increase with NP
651 concentration (*i.e.*, strictly, on the number of particles per unit volume). This prediction is
652 fulfilled by the results of Figure 7, which open up the possibility of targeting bacteria at different
653 stages of growth by carefully tuning the concentration of PC-NPs to the desired bacterial density.
654 For example, PC-NPs could be engineered for the precise release of bioactive molecules at a
655 certain stage of bacterial growth. A full understanding of the role of cell aggregation in the
656 appearance of the growth anomalies is required before this possibility can be developed into a
657 new technological approach for density-dependent bacterial manipulation.

658 PC-NPs displayed a QQ activity that is comparable to those of the ionically crosslinked IC-
659 NPs and raw CS preparations characterized earlier by our group (Table I) [42,65,66]. Interestingly,
660 the QQ activity of the dually crosslinked CC-NPs was much lower (Table I), further attesting to
661 the significance of the new fabrication method reported here. While the actual mechanism of
662 QS inhibition has not been described for any of these CS-based materials, it is reasonable to
663 think that a common mode of action could explain their QQ activity. Using the PC-NPs
664 described here as a representative example for all these materials, one could argue that NP
665 binding to the bacterial envelope may affect the uptake of nutrients and, as a result, the apparent
666 QQ activity would merely be the consequence of a general metabolic impairment. As discussed
667 above, the reduced OD_{600} values obtained in the presence of PC-NPs might not reflect decreased
668 growth, at least not to the levels suggested by the plots of Figure 5. Strikingly, the initial slope
669 of the burst in the fluorescence response curve (first 100 min after induction with AHL) obtained
670 in the presence of PC-NPs is not different from those obtained the absence of NPs. This is despite
671 of the fact that treated cells had been pre-incubated with PC-NPs for an hour before induction
672 (see Figures 5E-F and insets of Figures S4-6). This observation is in clear disagreement with the

idea that metabolic arrest was the main cause of the observed PC-NP-induced, endpoint reduction in FI/OD_{600}, as one would expect to see slower fluorescence accumulation immediately after AHL induction in metabolically arrested cells. In an alternative QQ mechanism, NPs could act as "chemical abductors", by sequestering AHL from the medium. However, the absence of dose dependence associated to the QQ activity displayed by PC-NPs, is in clear disagreement with their potential "AHL abducting" ability. This very lack of dose dependence, especially during the initial burst phase, also rules out a simple mechanism in which the coating of the external envelope with CS-NPs made the cells impermeable to AHLs. Perhaps the explanation to the QQ activity of PC-NPs might have to do with the direct perturbation of the QS machinery of the biosensor by the binding of CS-NPs to the bacterial envelope [65,69–71]. Kolibachuck and Greenberg published in 1993 a report in which they described LuxR as a membrane associated protein in its native *Vibrio fischeri* host [72]. This result was later confirmed for other related QS activators [72,73]. Considering these observations, the idea that a potential interference of envelope-bound, CS-based NPs with the membrane localization of LuxR could provide a reasonable explanation to our results. Despite the intrinsic appeal of this hypothesis, many issues remain to be elucidated, not the least of which is whether LuxR membrane localization holds true in the *E. coli* biosensor. Finally, while this and our previous work (refs) demonstrate the QQ potential of CS-based NPs, it remains to be seen whether this potential is applicable only to luxR-based systems or, by the contrary, if it could be expanded to other types of QS networks. Future studies should be aimed at studying the possibility of inhibiting QS-induced biofilm formation in both Gram-negative and Gram-positive bacteria. CS-based NPs could bear an enormous potential as biodegradable, antibiotic-free, antibacterial compounds that can be used against multidrug resistant pathogens such as *Staphylococcus aureus*, *Pseudomonas aeruginosa*, *Klebsiella pneumoniae*, etc.

CONCLUSIONS

Here, we present a simplified and robust method to fabricate chitosan nanoparticles (PC-NPs) by covalent crosslinking of chitosan with genipin close to the critical gelling condition, followed by the formation of chitosan nanoparticles by ionic gelation with TPP. This new approach enables the fabrication of nanoparticles with improved physico-chemical properties,higher physiological colloidal stability, and with strong QQ activity. By combining the colloidal stability of dually crosslinked (GNP/TPP) CS NPs with the QS inhibitory activity of mono crosslinked (TPP) CS NPs [42], this work represents an improved strategy over the previously reported methods to manipulate chitosan into small nanoparticles [66]. The mode of action of PC-NPs and related CS NPs is consistent with the existence of a SR of NP/bacterium at which the negative ζ-potential of the bacterial envelope is counteracted by the positive charge of the NPs (refs). The fact that the establishment of this SR displays clear dose dependence on bacterial density, as shown here, implies that PC-NPs could be ideal for applications in which the targeting of bacterial populations at specific cell densities is desired. Future work must entail efforts to understand how this cell-density dependence of bacterial targeting by PC-NPs (and related compounds) is established at the molecular level. We believe that the QQ capacity of CS-based NPs deserves further attention as part of the search for novel anti-QS strategies that can be used to counteract the growth of bacterial pathogens in the context of the current antibiotic crisis. This works also expands the available strategies for the design of nanomaterials with the potential to carry and deliver bioactive molecules.

721 Supporting information

722 Small deformation oscillatory rheological data, bacterial growth curves, CLSM images,
723 experimental design of chitosan-GNP TPP nanoparticles formulations and time-lapse CLSM
724 videos are available as supporting information.

725

726

727 ACKNOWLEDGMENTS

728 This work was supported by the FP7 IIF Marie Curie project entitled BioNanoSmart_DDS
729 (Contract No. 221111), and by funds for the Consolidation and structuration of competitive
730 research units (Competitive Reference Groups) (REF. 2010/18), from the Spain Institute of
731 Health "Carlos III" (Strategic Health Action, Project FIS PSI14/00059) and "Xunta de Galicia"
732 (Project Competitive Reference Groups, 2014/043-FEDER). CVS was supported by a pre-
733 doctoral fellowship of the Xunta de Galicia and by a FPU fellowship of the "Ministerio de
734 Educación y Ciencia" of Spain, by a research fellowship of the DAAD (Germany), and a
735 research fellowship of the Fundación Pedro Barrié de la Maza (Spain). We thank Christopher
736 Anderson and Mariana Leguia for providing plasmid pSB1A3-BBa_T9002, Carlos Bustamante
737 for his support during the optimization of the *E. coli* fluorescent biosensor. We are also grateful
738 to Antje von Schaewen for the generous access to the Safire Tecan-F129013 Microplate Reader.

739

740 ABBREVIATIONS

741 AHL, acyl homoserine lactone; AUC, area under the curve; CC-NPs, GNP-co-crosslinked, CS-
742 TPP NPs; CLSM, confocal laser scanning microscopy; CS, chitosan; CS NCs, CS-based
743 nanocapsules; DA, degree of acetylation; DLS-NIBS, dynamic light scattering with non-
744 invasive back scattering; FI, fluorescence intensity; FI/OD_{600}, density-normalized fluorescence
745 intensity; GFP, green fluorescent protein; GNP, genipin; IC-NPs, ionically crosslinked CS NPs;
746 PD, polymer polydispersity index; M3-PALS, phase analysis light scattering with mixed mode
747 measurements; MW, molecular weight; NPs, nanoparticles; OD_{600}, bacterial optical density;
748 PC-A, PC-NP prototype A; PC-B, PC-NP prototype B; PdI, particle polydispersity index; PC-

NPs, GNP-pre-crosslinked CS-TPP nanoparticles; NCs, nanocapsules; PT, Percolation Theory; QQ, quorum quenching; QS, quorum sensing; ROIs, regions of interest; SR, stoichiometric ratio; $t_{gel\text{-}DLS}$, critical gel time obtained by DLS-NIBS; TPP, sodium tripolyphosphate; $t_{gel\text{-}rheo}$, rheological critical gel time; ζ, zeta potential.

References

(1) Rinaudo, M. Chitin and Chitosan: Properties and Applications. *Prog. Polym. Sci.* **2006**, *31* (7), 603–632.

(2) Dash, M.; Chiellini, F.; Ottenbrite, R. M.; Chiellini, E. Chitosan—A Versatile Semi-Synthetic Polymer in Biomedical Applications. *Prog. Polym. Sci.* **2011**, *36* (8), 981–1014.

(3) Berger, J.; Reist, M.; Mayer, J. M.; Felt, O.; Peppas, N. A.; Gurny, R. Structure and Interactions in Covalently and Ionically Crosslinked Chitosan Hydrogels for Biomedical Applications. *Eur. J. Pharm. Biopharm.* **2004**, *57* (1), 19–34.

(4) Moura, M. J.; Faneca, H.; Lima, M. P.; Gil, M. H.; Figueiredo, M. M. In Situ Forming Chitosan Hydrogels Prepared via Ionic/Covalent Co-Cross-Linking. *Biomacromolecules* **2011**, *12* (9), 3275–3284.

(5) Jonassen, H.; Kjøniksen, A. L.; Hiorth, M. Effects of Ionic Strength on the Size and Compactness of Chitosan Nanoparticles. *Colloid Polym. Sci.* **2012**, *290* (10), 919–929.

(6) Calvo, P.; Remunan-Lopez, C.; Vila-Jato, J. .; Alonso, M. J. Novel Hydrophilic Chitosan-Polyethylene Oxide Nanoparticles as Protein Carriers. *J. Appl. Polym. Sci.* **1997**, *63*, 125–132.

(7) Liu, H.; Gao, C. Preparation and Properties of Ionically Cross-Linked Chitosan

Nanoparticles. *Polym. Adv. Technol.* **2009**, *20* (7), 613–619.

(8) Zhang, X.; Malhotra, S.; Molina, M.; Haag, R. Micro- and Nanogels with Labile Crosslinks - from Synthesis to Biomedical Applications. *Chem. Soc. Rev.* **2015**, *44* (7), 1948–1973.

(9) Kawashima, Y.; Handa, T.; Kasai, A.; Takenaka, H.; Lin, S. Y.; Ando, Y. Novel Method for the Preparation of Controlled-Release Theophylline Granules Coated with a Polyelectrolyte Complex of Sodium Polyphosphate-Chitosan. *J. Pharm. Sci.* **1985**, *74* (3), 264–268.

(10) Giri, T. K.; Thakur, A.; Alexander, A.; Badwaik, H.; Tripathi, D. K. Modified Chitosan Hydrogels as Drug Delivery and Tissue Engineering Systems: Present Status and Applications. *Acta Pharm. Sin. B* **2012**, *2* (5), 439–449.

(11) Lin, Y.-H.; Tsai, S.-C.; Lai, C.-H.; Lee, C.-H.; He, Z. S.; Tseng, G.-C. Genipin-Cross-Linked Fucose-Chitosan/Heparin Nanoparticles for the Eradication of Helicobacter Pylori. *Biomaterials* **2013**, *34* (18), 4466–4479.

(12) Zhang, Y.; Thomas, Y.; Kim, E.; Payne, G. F. PH- and Voltage-Responsive Chitosan Hydrogel through Covalent Cross-Linking with Catechol. *J. Phys. Chem. B* **2012**, *116* (5), 1579–1585.

(13) Espinosa-García, B. M.; Argüelles-Monal, W. M.; Hernández, J.; Félix-Valenzuela, L.; Acosta, N.; Goycoolea, F. M. Molecularly Imprinted Chitosan-Genipin Hydrogels with Recognition Capacity toward o-Xylene. *Biomacromolecules* **2007**, *8*, 3355–3364.

(14) Butler, M. F.; Ng, Y.-F.; Pudney, P. D. A. Mechanism and Kinetics of the Crosslinking

Reaction between Biopolymers Containing Primary Amine Groups and Genipin. *J. Polym. Sci. Part A Polym. Chem.* **2003**, *41* (24), 3941–3953.

(15) Mi, F. L.; Sung, H. W.; Shyu, S. S. Synthesis and Characterization of a Novel Chitosan-Based Network Prepared Using Naturally Occurring Crosslinker. *J. Polym. Sci. Part A Polym. Chem.* **2000**, *38* (15), 2804–2814.

(16) Muzzarelli, R. A. A. Genipin-Crosslinked Chitosan Hydrogels as Biomedical and Pharmaceutical Aids. *Carbohydr. Polym.* **2009**, *77* (1), 1–9.

(17) Yuan, Y.; Chesnutt, B. M.; Utturkar, G.; Haggard, W. O.; Yang, Y.; Ong, J. L.; Bumgardner, J. D. The Effect of Cross-Linking of Chitosan Microspheres with Genipin on Protein Release. *Carbohydr. Polym.* **2007**, *68* (3), 561–567.

(18) Klein, M. P.; Hackenhaar, C. R.; Lorenzoni, A. S. G.; Rodrigues, R. C.; Costa, T. M. H.; Ninow, J. L.; Hertz, P. F. Chitosan Crosslinked with Genipin as Support Matrix for Application in Food Process: Support Characterization and β-d-Galactosidase Immobilization. *Carbohydr. Polym.* **2016**, *137*, 184–190.

(19) Song, X.; Wu, H.; Li, S.; Wang, Y.; Ma, X.; Tan, M. Ultrasmall Chitosan–Genipin Nanocarriers Fabricated from Reverse Microemulsion Process for Tumor Photothermal Therapy in Mice. *Biomacromolecules* **2015**, *16* (7), 2080–2090.

(20) Harris, R.; Lecumberri, E.; Heras, A. Chitosan-Genipin Microspheres for the Controlled Release of Drugs: Clarithromycin, Tramadol and Heparin. *Mar. Drugs* **2010**, *8* (6), 1750–1762.

(21) Chen, H.; Wei, O.; Martoni, C.; Prakash, S. Genipin Cross-Linked Polymeric Alginate-

814 Chitosan Microcapsules for Oral Delivery: In-Vitro Analysis. *Int. J. Polym. Sci.* **2009**,
815 *Volume 200*, Article ID 617184, 16 pages.

816 (22) Bassler, B. L.; Losick, R. Bacterially Speaking. *Cell* **2006**, *125* (2), 237–246.

817 (23) Rutherford, S. T.; Bassler, B. L. Bacterial Quorum Sensing: Its Role in Virulence and
818 Possibilities for Its Control. *Cold Spring Harb. Perspect. Med.* **2012**, *2* (11), a012427.

819 (24) Ng, W. L.; Bassler, B. L. Bacterial Quorum-Sensing Network Architectures. *Ann Rev*
820 *Genet* **2009**, *43*, 197–222.

821 (25) Taga, M. E.; Bassler, B. L. Chemical Communication among Bacteria. *Proc. Natl. Acad.*
822 *Sci. U. S. A.* **2003**, *100* (2), 14549–14554.

823 (26) Churchill, M. E. A.; Chen, L. Structural Basis of Acyl-Homoserine Lactone-Dependent
824 Signaling. *Chem. Rev.* **2011**, *111* (1), 68–85.

825 (27) Fuqua, C.; Greenberg, E. P. Listening in on Bacteria: Acyl-Homoserine Lactone
826 Signalling. *Nat. Rev. Mol. Cell Biol.* **2002**, *3* (9), 685–695.

827 (28) Koch, B.; Liljefors, T.; Persson, T.; Nielsen, J.; Kjelleberg, S.; Givskov, M. The LuxR
828 Receptor: The Sites of Interaction with Quorum-Sensing Signals and Inhibitors.
829 *Microbiology* **2005**, *151* (11), 3589–3602.

830 (29) Qin, N.; Callahan, S. M.; Dunlap, P. V; Stevens, A. M. Analysis of LuxR Regulon Gene
831 Expression during Quorum Sensing in Vibrio Fischeri. *J. Bacteriol.* **2007**, *189* (11),
832 4127–4134.

833 (30) LaSarre, B.; Federle, M. J. Exploiting Quorum Sensing To Confuse Bacterial Pathogens.

Microbiol. Mol. Biol. Rev. **2013**, *77* (1), 73–111.

(31) Gonzalez, J. E.; Keshavan, N. D. Messing with Bacterial Quorum Sensing. *Microbiol. Mol. Biol. Rev.* **2006**, *70* (4), 859–875.

(32) Christensen, Q. H.; Grove, T. L.; Booker, S. J.; Greenberg, E. P. A High-Throughput Screen for Quorum-Sensing Inhibitors That Target Acyl-Homoserine Lactone Synthases. *Proc. Natl. Acad. Sci. U. S. A.* **2013**, *110* (34), 13815–13820.

(33) Romero, M.; Acuña, L.; Otero, A. Patents on Quorum Quenching: Interfering with Bacterial Communication as a Strategy to Fight Infections. *Recent Pat. Biotechnol.* **2012**, *6* (1), 2–12.

(34) Manefield, M.; Rasmussen, T. B.; Henzter, M.; Andersen, J. B.; Steinberg, P.; Kjelleberg, S.; Givskov, M. Halogenated Furanones Inhibit Quorum Sensing through Accelerated LuxR Turnover. *Microbiology* **2002**, *148* (Pt 4), 1119–1127.

(35) Mayer, C.; Romero, M.; Muras, A.; Otero, A. Aii20J, a Wide-Spectrum Thermostable N-Acylhomoserine Lactonase from the Marine Bacterium Tenacibaculum Sp. 20J, Can Quench AHL-Mediated Acid Resistance in Escherichia Coli. *Appl. Microbiol. Biotechnol.* **2015**, *99* (22), 9523–9539.

(36) Piletska, E. V; Stavroulakis, G.; Larcombe, L. D.; Whitcombe, M. J.; Sharma, A.; Primrose, S.; Robinson, G. K.; Piletsky, S. A. Passive Control of Quorum Sensing: Prevention of Pseudomonas Aeruginosa Biofilm Formation by Imprinted Polymers. *Biomacromolecules* **2011**, *12* (4), 1067–1071.

(37) Cavaleiro, E.; Chianella, I.; Whitcombe, M. J.; Piletsky, S. A.; Correia, A.; Duarte, A. S.

Synthetic Polymers Capable of Suppressing Virulence of Bacterial Fish Pathogens. *Curr. Opin. Biotechnol.* **2011**, *22*, S79–S79.

(38) Piras, A. M.; Maisetta, G.; Sandreschi, S.; Gazzarri, M.; Bartoli, C.; Grassi, L.; Esin, S.; Chiellini, F.; Batoni, G. Chitosan Nanoparticles Loaded with the Antimicrobial Peptide Temporin B Exert a Long-Term Antibacterial Activity in Vitro against Clinical Isolates of Staphylococcus Epidermidis. *Front. Microbiol.* **2015**, *6*, 372.

(39) Gupta, A.; Terrell, J. L.; Fernandes, R.; Dowling, M. B.; Payne, G. F.; Raghavan, S. R.; Bentley, W. E. Encapsulated Fusion Protein Confers "Sense and Respond" Activity to Chitosan-Alginate Capsules to Manipulate Bacterial Quorum Sensing. *Biotechnol. Bioeng.* **2013**, *110* (2), 552–562.

(40) Cobrado, L.; Azevedo, M. M.; Silva-Dias, A.; Ramos, J. P.; Pina-Vaz, C.; Rodrigues, A. G. Cerium, Chitosan and Hamamelitannin as Novel Biofilm Inhibitors? *J. Antimicrob. Chemother.* **2012**, *67* (5), 1159–1162.

(41) Costa, E. M.; Silva, S.; Pina, C.; Tavaria, F. K.; Pintado, M. Antimicrobial Effect of Chitosan against Periodontal Pathogens Biofilms. *SOJ Microbiol Infect Dis* **2014**, *2* (1), 1–6.

(42) Vila-Sanjurjo, C.; David, L.; Remuñán-López, C.; Vila-Sanjurjo, A.; Goycoolea, F. M. Effect of the Ultrastructure of Chitosan Nanoparticles in Colloidal Stability, Quorum Quenching and Antibacterial Activities. *J. Colloid Interface Sci.* **2019**, *556*, 592–605. https://doi.org/10.1016/j.jcis.2019.08.061.

(43) Tanaka, K.; Nishida, K.; Gabrys, B.; J. Lawrence, M.; Kanaya, T. Critical Dissolution

Ionic Strength of Aqueous Solution of Chitosan Hydrochloride Salt. *Sen-i Gakkaishi (Journal Soc. Fiber Sci. Technol. Japan* **2014**, *70*, 225–231.

(44) Stauffer, D.; Coniglio, A.; Adam, M. Gelation and Critical Phenomena. In *Polymer Networks*; Dušek, K., Ed.; Springer Berlin Heidelberg: Berlin, Heidelberg, 1982; pp 103–158.

(45) de Morais, W. A.; Pereira, M. R.; Fonseca, J. L. C. Characterization of Gelification of Chitosan Solutions by Dynamic Light Scattering. *Carbohydr. Polym.* **2012**, *87* (4), 2376–2380.

(46) Stauffer, D.; Aharony, A. Cluster Numbers. In *Introduction to Percolation Theory.*; Stauffer, D., Aharony, A., Eds.; London: UK Taylor & Francis Ltd., 1994; pp 15–59.

(47) Sauerwald, T.; Hennemann, J.; Kohl, C.-D.; Wagner, T.; Russ, S. H2S Detection Utilizing Percolation Effects in Copper Oxide. In *Proc Sens 2013*; 2013; pp 656–660.

(48) Kurselis, K.; Kiyan, R.; Bagratashvili, V. N.; Popov, V. K.; Chichkov, B. N. 3D Fabrication of All-Polymer Conductive Microstructures by Two Photon Polymerization. *Opt. Express* **2013**, *21* (25), 31029–31035.

(49) Vila-Sanjurjo, C.; Engwer, C.; Qin, X.; Hembach, L.; Verdía-Cotelo, T.; Remuñán-López, C.; Vila-Sanjurjo, A.; Goycoolea, F. M. A Single Intracellular Protein Governs the Critical Transition from an Individual to a Coordinated Population Response during Quorum Sensing: Origins of Primordial Language. *bioRxiv* **2016**.

(50) Tung, C.-Y. M.; Dynes, P. J. Relationship between Viscoelastic Properties and Gelation in Thermosetting Systems. *J. Appl. Polym. Sci.* **1982**, *27* (2), 569–574.

(51) Engwer, C.; Loy, R.; Chronakis, I. S.; Mendes, C.; Francisco, M. Mesoscopic Gelation of Chitosan and Genipin at below Critical Concentrations. *ChemRxiv* **2017**, 1–10. https://doi.org/10.26434/chemrxiv.5487172.v1.

(52) Carvalho, E. L. S.; Grenha, A.; Remuñán-López, C.; Alonso, M. J.; Seijo, B. Mucosal Delivery of Liposome–Chitosan Nanoparticle Complexes. *Methods Enzymol.* **2009**, *465*, 289–312.

(53) Canton, B.; Labno, A.; Endy, D. Refinement and Standardization of Synthetic Biological Parts and Devices. *Nat. Biotechnol.* **2008**, *26* (7), 787–793.

(54) Oslizlo, A.; Stefanic, P.; Dogsa, I.; Mandic-Mulec, I. Private Link between Signal and Response in Bacillus Subtilis Quorum Sensing. *Proc. Natl. Acad. Sci. U. S. A.* **2014**, *111* (4), 1586–1591.

(55) Tan, S. Y.-Y.; Chua, S.-L.; Chen, Y.; Rice, S. A.; Kjelleberg, S.; Nielsen, T. E.; Yang, L.; Givskov, M. Identification of Five Structurally Unrelated Quorum-Sensing Inhibitors of Pseudomonas Aeruginosa from a Natural-Derivative Database. *Antimicrob. Agents Chemother.* **2013**, *57* (11), 5629–5641.

(56) Shibayama, M. Universality and Specificity of Polymer Gels Viewed by Scattering Methods. *Bull. Chem. Soc. Jpn.* **2006**, *79* (12), 1799–1819.

(57) Dmour, I.; Taha, M. O. Novel Nanoparticles Based on Chitosan-Dicarboxylate Conjugates via Tandem Ionotropic/Covalent Crosslinking with Tripolyphosphate and Subsequent Evaluation as Drug Delivery Vehicles. *Int. J. Pharm.* **2017**, *529* (1–2), 15–31.

(58) Huang, Y.; Lapitsky, Y. Salt-Assisted Mechanistic Analysis of Chitosan/Tripolyphosphate Micro- and Nanogel Formation. *Biomacromolecules* **2012**, *13* (11), 3868–3876.

(59) Huang, Y.; Lapitsky, Y. Monovalent Salt Enhances Colloidal Stability during the Formation of Chitosan/Tripolyphosphate Microgels. *Langmuir* **2011**, *27* (17), 10392–10399.

(60) Huang, Y.; Lapitsky, Y. On the Kinetics of Chitosan/Tripolyphosphate Micro- and Nanogel Aggregation and Their Effects on Particle Polydispersity. *J. Colloid Interface Sci.* **2017**, *486*, 27–37.

(61) Yang, H.-C.; Hon, M.-H. The Effect of the Degree of Deacetylation of Chitosan Nanoparticles and Its Characterization and Encapsulation Efficiency on Drug Delivery. *Polym. Plast. Technol. Eng.* **2010**, *49* (12), 1292–1296.

(62) Sreekumar, S.; Goycoolea, F. M.; Moerschbacher, B. M.; Rivera-Rodriguez, G. R. Parameters Influencing the Size of Chitosan-TPP Nano- and Microparticles. *Sci. Rep.* **2018**, *8* (1), 4695.

(63) Razi, M. A.; Wakabayashi, R.; Tahara, Y.; Goto, M.; Kamiya, N. Genipin-Stabilized Caseinate-Chitosan Nanoparticles for Enhanced Stability and Anti-Cancer Activity of Curcumin. *Colloids Surfaces B Biointerfaces* **2018**, *164*, 308–315.

(64) Mohammed, M. A.; Syeda, J. T. M.; Wasan, K. M.; Wasan, E. K. An Overview of Chitosan Nanoparticles and Its Application in Non-Parenteral Drug Delivery. *Pharmaceutics* **2017**, *9* (4). https://doi.org/10.3390/pharmaceutics9040053.

939 (65) Qin, X.; Engwer, C.; Desai, S.; Vila-Sanjurjo, C.; Goycoolea, F. M. An Investigation of
940 the Interactions between an E. Coli Bacterial Quorum Sensing Biosensor and Chitosan-
941 Based Nanocapsules. *Colloids Surfaces B Biointerfaces* **2017**, *149*, 358–368.

942 (66) Qin, X.; Emich, J.; Goycoolea, F. Assessment of the Quorum Sensing Inhibition Activity
943 of a Non-Toxic Chitosan in an N-Acyl Homoserine Lactone (AHL)-Based Escherichia
944 Coli Biosensor. *Biomolecules* **2018**, *8* (3), 87.

945 (67) Costalat, M.; David, L.; Delair, T. Reversible Controlled Assembly of Chitosan and
946 Dextran Sulfate: A New Method for Nanoparticle Elaboration. *Carbohydr. Polym.* **2014**,
947 *102* (1), 717–726.

948 (68) Masarudin, M. J.; Cutts, S. M.; Evison, B. J.; Phillips, D. R.; Pigram, P. J. Factors
949 Determining the Stability, Size Distribution, and Cellular Accumulation of Small,
950 Monodisperse Chitosan Nanoparticles as Candidate Vectors for Anticancer Drug
951 Delivery: Application to the Passive Encapsulation of [14C]-Doxorubicin. *Nanotechnol.*
952 *Sci. Appl.* **2015**, *8*, 67.

953 (69) Helander, I. .; Nurmiaho-Lassila, E.-L.; Ahvenainen, R.; Rhoades, J.; Roller, S. Chitosan
954 Disrupts the Barrier Properties of the Outer Membrane of Gram-Negative Bacteria. *Int.*
955 *J. Food Microbiol.* **2001**, *71* (2–3), 235–244.

956 (70) Jeon, S. J.; Oh, M.; Yeo, W.-S.; Galvão, K. N.; Jeong, K. C. Underlying Mechanism of
957 Antimicrobial Activity of Chitosan Microparticles and Implications for the Treatment of
958 Infectious Diseases. *PLoS One* **2014**, *9* (3), e92723.

959 (71) Fernandes, M. M.; Francesko, A.; Torrent-Burgués, J.; Carrión-Fité, F. J.; Heinze, T.;

960 Tzanov, T. Sonochemically Processed Cationic Nanocapsules: Efficient Antimicrobials
961 with Membrane Disturbing Capacity. *Biomacromolecules* **2014**, *15* (4), 1365–1374.

962 (72) Kolibachuk, D.; Greenberg, E. P. The Vibrio Fischeri Luminescence Gene Activator
963 LuxR Is a Membrane-Associated Protein. *J. Bacteriol.* **1993**, *175* (22), 7307–7312.

964 (73) Qin, Y.; Luo, Z.-Q.; Smyth, A. J.; Gao, P.; Beck von Bodman, S.; Farrand, S. K. Quorum-
965 Sensing Signal Binding Results in Dimerization of TraR and Its Release from Membranes
966 into the Cytoplasm. *EMBO J.* **2000**, *19* (19), 5212–5221.
967 https://doi.org/10.1093/emboj/19.19.5212.

968 (74) Thoendel, M.; Horswill, A. R. Identification of Staphylococcus Aureus AgrD Residues
969 Required for Autoinducing Peptide Biosynthesis. *J. Biol. Chem.* **2009**, *284* (33), 21828–
970 21838.

971 (75) Kaur, G.; Balamurugan, P.; Adline Princy, S. Inhibition of the Quorum Sensing System
972 (ComDE Pathway) by Aromatic 1,3-Di-m-Tolylurea (DMTU): Cariostatic Effect with
973 Fluoride in Wistar Rats. *Front. Cell. Infect. Microbiol.* **2017**, *7* (JUL), 313.

974 (76) Pang, Z.; Raudonis, R.; Glick, B. R.; Lin, T. J.; Cheng, Z. Antibiotic Resistance in
975 Pseudomonas Aeruginosa: Mechanisms and Alternative Therapeutic Strategies.
976 *Biotechnology Advances*. 2019, pp 177–192.

977 (77) Chambers, H. F.; DeLeo, F. R. Waves of Resistance: Staphylococcus Aureus in the
978 Antibiotic Era. *Nature Reviews Microbiology*. 2009, pp 629–641.

979

980

TABLE OF CONTENTS GRAPHIC